Discovery and functional characterization of a neomorphic PTEN mutation

Helio A. Costa[a], Michael G. Leitner[b], Martin L. Sos[c,d,1], Angeliki Mavrantoni[b], Anna Rychkova[a], Jeffrey R. Johnson[c,e], Billy W. Newton[c,e], Muh-Ching Yee[a], Francisco M. De La Vega[a], James M. Ford[a], Nevan J. Krogan[c,e], Kevan M. Shokat[c,d], Dominik Oliver[b], Christian R. Halaszovich[b,2], and Carlos D. Bustamante[a,2]

[a]Department of Genetics, Stanford University School of Medicine, Stanford, CA 94305; [b]Department of Neurophysiology, Philipps-Universität Marburg, 35037 Marburg, Germany; [c]Department of Cellular and Molecular Pharmacology, University of California, San Francisco, CA 94158; [d]Howard Hughes Medical Institute, San Francisco, CA 94158; and [e]J. David Gladstone Institutes, San Francisco, CA 94158

Although a variety of genetic alterations have been found across cancer types, the identification and functional characterization of candidate driver genetic lesions in an individual patient and their translation into clinically actionable strategies remain major hurdles. Here, we use whole genome sequencing of a prostate cancer tumor, computational analyses, and experimental validation to identify and predict novel oncogenic activity arising from a point mutation in the phosphatase and tensin homolog (PTEN) tumor suppressor protein. We demonstrate that this mutation (p.A126G) produces an enzymatic gain-of-function in PTEN, shifting its function from a phosphoinositide (PI) 3-phosphatase to a phosphoinositide (PI) 5-phosphatase. Using cellular assays, we demonstrate that this gain-of-function activity shifts cellular phosphoinositide levels, hyperactivates the PI3K/Akt cell proliferation pathway, and exhibits increased cell migration beyond canonical PTEN loss-of-function mutants. These findings suggest that mutationally modified PTEN can actively contribute to well-defined hallmarks of cancer. Lastly, we demonstrate that these effects can be substantially mitigated through chemical PI3K inhibitors. These results demonstrate a new dysfunction paradigm for PTEN cancer biology and suggest a potential framework for the translation of genomic data into actionable clinical strategies for targeted patient therapy.

functional genomics | PTEN | tumor suppressor

The application of next generation sequencing in cancer biology has produced a deluge of genomic alterations present across human cancers (1, 2). This information has helped identify common mutational signatures in cancer types and subtypes (3–5). However, application of systematic patient-specific sequencing data to guide personalized cancer treatment has been limited in practice (6–8). The key challenge is functional understanding of the individual genetic lesions in the given phenotypic context and its translation into actionable strategies for targeted treatment.

To test the utility of an unbiased computational and experimental framework in causal variant identification and characterization, we sequenced to high coverage the entirety of a prostate tumor biopsy and its matched normal (buccal) tissue from a 59-y-old Hispanic male with aggressive prostate adenocarcinoma [stage T3a; Gleason score 7 (4+3)] (*SI Appendix*, Fig. S1A).

Results

Whole-Genome Sequencing of Prostate Cancer Sample Identifies Mutant PTEN.
Paired-end Illumina 100-base pair (bp) reads were mapped to the reference genome, and, after quality filtering, realignment, and recalibration, the average fold-coverage of tumor and normal tissue was 98× and 47×, respectively (*SI Appendix*, Table S1). We developed a somatic variant-calling pipeline to comprehensively characterize single nucleotide variants (SNVs), insertions/deletions (INDELs), structural variation (SV), and copy number variants (CNVs) present uniquely within the tumor genome (*SI Appendix*, Fig. S2). This approach allows for detection of novel driver lesions within a patient that are overlooked by targeted SNV

panels focusing on known mutations of a few dozen genes. We identified a total of 6,050 tumor-specific variants consisting of 4,823 SNVs, 356 INDELs, 867 copy number variants, and four structural variants (Table 1). We note that the allelic fraction distribution of detected SNVs had an upper quartile value of 20%, which is in line with pathological estimates of ~15% tumor purity (*SI Appendix*, Fig. S1 A and B). We manually curated all structural variants and any copy number variants within coding or regulatory regions. In parallel, to prioritize potentially pathogenic SNV and INDEL mutations, we focused on rare (≤2% 1,000 Genomes global allele frequency) variants that were predicted to be deleterious coding or regulatory mutations (Table 1). After applying this stringent set of criteria, we were left with a total of 12 candidate driver mutations to further investigate (*SI Appendix*, Table S2).

PTEN p.A126G Is Predicted to Alter Protein Function.
Manual curation of the 12 variants identified a nonsynonymous somatic substitution predicted to convert alanine to glycine at amino acid 126

Significance

Identification of putative functional genetic mutations involved in cancer has been dramatically accelerated by developments in next generation sequencing technologies. However, analyzing an individual patient genome and interpreting mutation spectra to inform cancer origin and targeted treatment have been challenging. This study presents a framework interpreting a single patient's genome and identifies a novel causal mutation in the phosphatase and tensin homolog (PTEN) tumor suppressor. Through computational and experimental approaches, we demonstrate that this mutation causes PTEN to retain known tumor suppressor function while gaining protumor activity. This finding suggests a new role for PTEN and other tumor suppressor involvement in cancer formation and reveals the potential wealth of biological information currently underexploited by the lack of systematic approaches for cancer genome interpretation services.

Table 1. Number of somatic candidate variants based on filtering strategy

Filter	SNV	INDEL	CNV	SV
Total somatic variants	4,823	356	867	4
Somatic variants within coding or regulatory region	367	12	4	0
Somatic variants and ≤2% AF in 1000G or ESP	358	12	0	0
Somatic variants and either nonsynonymous SNV or splice site donor/acceptor SNV or coding INDEL	28	1	0	0
Somatic variants and predicted damaging by SIFT and/or PolyPhen2	12	0	0	0

1000G, 1,000 Genomes Project; AF, allele frequency; ESP, NHLBI Exome Sequencing Project.

(p.A126G) of the PTEN protein. Given the well-characterized role of PTEN as an important modulator of prostate cancer growth (9) and the location of the mutation in the active site of the PTEN protein, we prioritized this genetic lesion as the top candidate driver mutation. Interestingly, this mutation has been detected in an invasive breast carcinoma case within The Cancer Genome Atlas database (case ID: TCGA-LL_A5YP) (2) but has remained uncharacterized or targeted in extant somatic variant detection platforms (Illumina TruSeq Amplicon v1 or Ion AmpliSeq v2). PTEN is a commonly mutated tumor suppressor that, by dephosphorylating $PI(3,4,5)P_3$ (PIP$_3$) and $PI(3,4)P_2$ to $PI(4,5)P_2$ and $PI(4)P$, respectively, functions as a phosphoinositide (PI) 3-phosphatase, inhibiting the PI3K/Akt pathway controlling cellular proliferation, metabolism, and growth (10, 11). Studies have shown that decreased activity or loss of PTEN can elicit cancer phenotypes so it is traditionally classified as a tumor suppressor gene (i.e., a gene where loss-of-function mutations lead to oncogenesis) (12). However, recent work suggests a more expansive role for PTEN in cancer biology. For example, mutant PTEN alleles have been shown to inhibit WT PTEN activity by interacting in a dominant negative manner (13). Amino acid 126 (Fig. 1*A*, green) is within the highly conserved catalytic "P-loop" site of PTEN and is two amino acids away from the catalytic cysteine at residue 124 (purple) (Fig. 1 *A* and *B*). Curiously, the p.A126G mutation produces a binding pocket amino acid sequence identical to VSP family proteins (14–16), which are PTEN-homologous phosphoinositide 5-phosphatases (17) (Fig. 1*C*). Although the mutation does not clearly disrupt the P-loop (Fig. 1*D*), mutant homology with VSPs led us to hypothesize a change in substrate specificity for the mutant form of PTEN. To this end, we used the $Ins(1,3,5)P_4$ molecule to model $PI(3,4,5)P_3$, calculating binding free energies of 3- and 5-oriented substrate in the PTEN WT and mutant binding pockets.

Using the available crystal structure of PTEN bound to L(+)-tartrate (18), we obtained docking coordinates for the $Ins(1,3,5)P_4$ substrate. $Ins(1,3,5)P_4$ was superimposed with the tartrate molecule to orient it with either the 5- or 3-phosphate positioned in the catalytic site (*SI Appendix*, Fig. S3 *A* and *B*). Our calculations, based on these simulations of binding free energy, show that the WT active site thermodynamically favors a 3-oriented substrate whereas the mutant p.A126G allele prefers a 5-oriented substrate (Fig. 1*E* and *SI Appendix*, Fig. S3*C*). Further, we repeated these analyses on other reported residue 126 somatic mutations (COSMIC v64) (1) and found that none were predicted to produce the gain-of-function activity identified in the A126G PTEN mutant (Fig. 1*E* and *SI Appendix*, Fig. S3*C*). These results suggest that p.A126G shifts binding preference toward 5- rather than 3-oriented phosphoinositides, causing a shift in PTEN enzymatic specificity.

Live-Cell Functional Assays Demonstrate That PTEN p.A126G Is a 5-Phosphatase. To validate the prediction that p.A126G shifts PTEN from a 3- to 5-phosphatase, we performed in vivo enzymatic assays using PTEN phosphoinositide substrates to assess the activity of WT, catalytically dead (p.C124S), and mutant (p.A126G) PTEN proteins. We performed these experiments by creating a voltage-dependent VSP-PTEN chimera (19, 20) that we can selectively activate and monitor for changes of phosphoinositide levels in living cells (Fig. 2*A*). When activated by depolarization, p.A126G PTEN (Fig. 2*B*, in green) shows the ability to reduce $PI(3,4,5)P_3$ levels, albeit at a reduced rate relative to WT (in black) (Fig. 2*B*). However, p.A126G PTEN produces $PI(3,4)P_2$ whereas WT depletes it (Fig. 2*C*). Unlike VSP phosphatases, $PI(4,5)P_2$ levels remain unchanged during activation in our engineered p.A126G PTEN, suggesting that
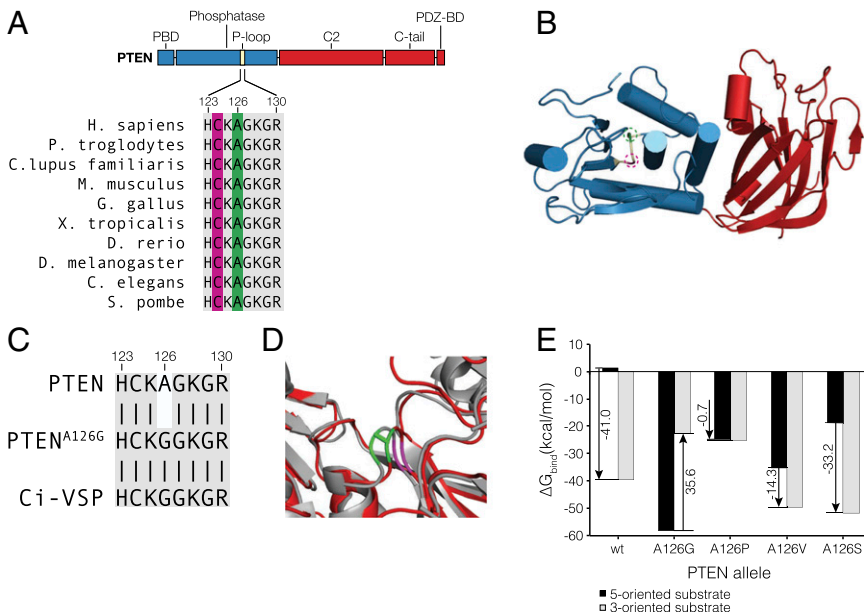

Fig. 1. Summary of PTEN amino acid 126. (*A*) PTEN domains and catalytic site (P-loop) conservation across species. PTEN is a 403-amino acid protein with five functional domains. The catalytic "P-loop" region (yellow) spans amino acids 123–130 and is completely conserved across a broad range of eukaryotes. The catalytic cysteine residue at position 124 is highlighted in purple, and amino acid 126 is highlighted in green. (*B*) PTEN protein structure with catalytic P-loop, residue 124, and residue 126 highlighted in yellow, purple and green, respectively. (*C*) Amino acid comparison of the catalytic CX$_5$R motif between WT PTEN, PTEN^{A126G}, and Ci-VSP. Gray boxes represent conserved regions. (*D*) PTEN WT (red) and p.A126G (gray) binding pocket overlay. (*E*) Binding free energies of 5- and 3-oriented $Ins(1,3,5)P_4$ to different PTEN alleles. Arrows indicate the direction of $\Delta\Delta G^{5\to3}_{bind}$.

the mutation had no detectable activity toward PI(4,5)P$_2$ (Fig. 2D). To demonstrate the specificity of the signals, a phosphatase-dead PTEN mutant (p.C124S) is shown (Fig. 2 B and C, purple). Further, we repeated these experiments on other reported residue 126 somatic mutations (COSMIC v64) (1) and found that none produced the gain-of-function activity identified in the p.A126G PTEN mutant (Fig. 2 E and F). Additionally, we performed ELISAs measuring cellular PI(3,4,5)P$_3$ and PI(3,4)P$_2$ levels in PTEN-null prostate cancer cells (PC-3) transiently expressing canonical WT, catalytic dead (p.C124S), and mutant (p.A126G) PTEN (Fig. 3 A and B). We found that p.A126G PTEN significantly decreases PI(3,4,5)P$_3$ (Fig. 3A) ($P \leq 0.05$) and increases PI(3,4)P$_2$ (Fig. 3B) ($P \leq 0.05$) relative to the catalytic dead p.C124S allele, consistent with our initial findings. These results suggest that the p.A126G mutation shifts PTEN enzymatic specificity from a 3- to a 5- phosphatase.

Novel PTEN 5-Phosphatase Mutant Activity Disrupts PI3K/Akt Signaling and Cell Migration. To assess the sole impact of the p.A126G PTEN enzymatic specificity change on the regulation of PI3K/Akt cellular signaling, we transiently expressed WT, catalytic dead (p.C124S), and mutant (p.A126G) PTEN in PTEN-null PC-3 cells. We found that p.A126G PTEN significantly increases phospho-Akt and phospho-S6 levels in the cell relative to WT (Fig. 3 C–E). These results demonstrate hyperactivation of the PI3K/Akt pathway, which is associated with tumorigenic phenotypes, including increased cell proliferation and reduced cellular apoptosis; they are consistent with our findings that p.A126G exhibits a decreased

ability to reduce PI(3,4,5)P$_3$ relative to WT (Fig. 2B). Importantly, we note that treatment with isoform-specific inhibitors of PI3K, predicted to antagonize loss of PTEN-mediated dephosphorylation of PI(3,4,5)P$_3$, are capable of restoring Akt and S6 phosphorylation to near WT levels (21). Further, to ensure no bias in characterizing the effect of the p.A126G mutation on global phosphorylation levels, we performed mass spectrometry on purified phosphopeptides of PC-3 cells transiently expressing catalytic dead (p.C124S) and mutant (p.A126G) PTEN (*SI Appendix*, Fig. S4 *A and B*). We then performed differential phosphoprotein abundance analysis on p.A126G-expressing cells, using catalytic dead (p.C124S)-expressing cells as the background. We identified a total of 601 enriched and 497 depleted (at least twofold) phosphopeptides relative to the catalytic dead background (*SI Appendix*, Fig. S4C). We note that, of the two PH-domain–containing PIP$_3$-regulated proteins expressed in PC-3 cells (Akt and PDK1), only phospho-Akt is seen above twofold enrichment. This finding is consistent with the above Akt Western blots demonstrating aberrant phospho-Akt expression in mutant cells. *SI Appendix*, Table S7 lists PH-domain–containing phosphopeptides enriched or depleted greater than twofold relative to p.C124S. To identify common processes and pathways that are enriched within the total pool of identified phosphopeptides, we performed GO-enrichment annotation clustering (*SI Appendix*, Tables S5 and S6). *SI Appendix*, Fig. S4D provides a selected subset of the most enriched statistically significant ($P \leq 0.05$) annotation clusters in p.A126G-expressing cells. We found enrichment of PTEN-regulated downstream pathways and processes, including the cancer-associated mTOR
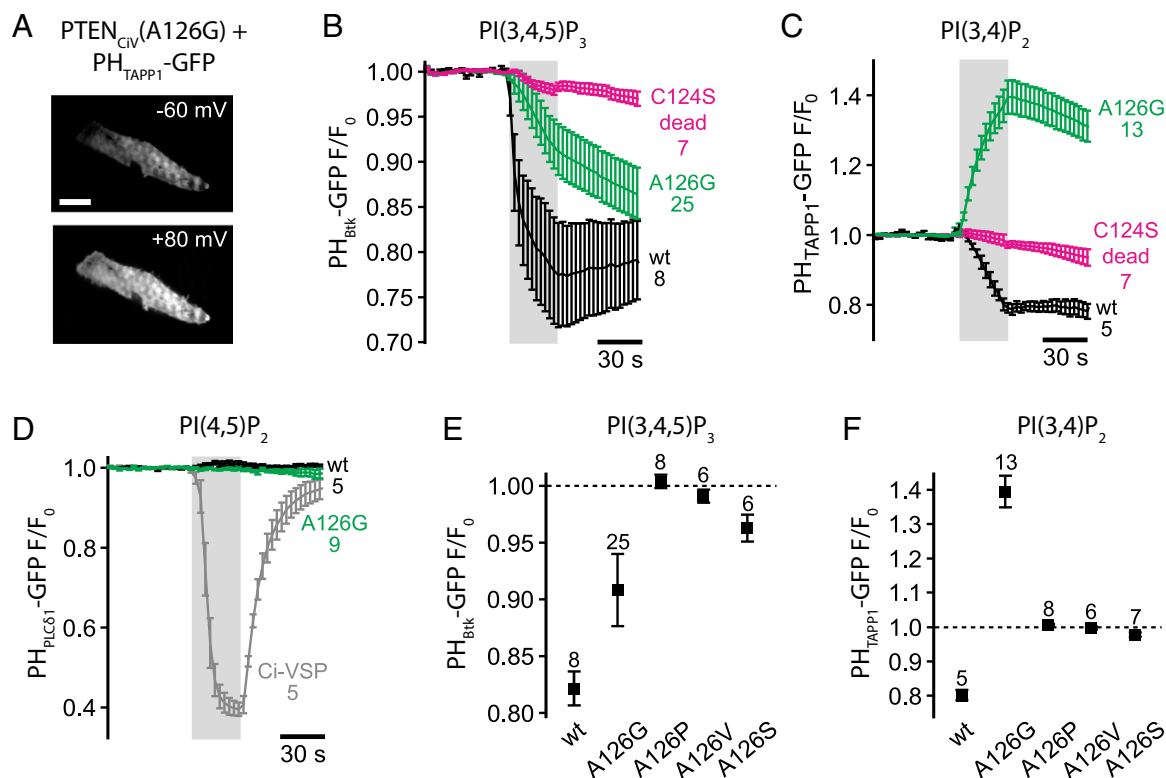

Fig. 2. Characterization of the phosphatase activity of PTEN A126 mutants. (A) Representative total internal reflection fluorescence (TIRF) images of a CHO cell coexpressing PTEN$_{CiV}$(A126G) and PH$_{TAPP1}$-GFP acquired before (*Top*) and during (*Bottom*) depolarization by whole-cell voltage clamp. (Scale bar: 10 μm.) *Insets* denote holding potential. The fluorescence intensity directly correlates to the amount of membrane-associated PH$_{TAPP1}$-GFP and thus reports on PI(3,4)P$_2$ levels. (B–D) Time course of TIRF signals in response to depolarization from a holding potential of –60 mV to +80 mV (gray shading) from cells expressing PTEN$_{CiV}$(A126G), catalytically inactivated (dead) PTEN$_{CiV}$(C124S), or PTEN$_{CiV}$(wild type/wt) with either (B) PI(3,4,5)P$_3$ sensor PH$_{Btk}$-GFP, (C) PI(3,4)P$_2$ sensor PH$_{TAPP1}$-GFP, or (D) PI(4,5)P$_2$ sensor PH$_{PLCδ1}$-GFP. In D, data from cells coexpressing PH$_{PLCδ1}$-GFP together with the PI(4,5)P$_2$-5-phosphatase Ci-VSP are included for comparison. Decrease and increase of fluorescence signal indicate, respectively, dissociation and association of the probes from and to the membrane. (E and F) Summary data on phosphatase activity of several PTEN A126 mutations. Note that only PTEN$_{CiV}$(A126G) produced PI(3,4)P$_2$ from PI(3,4,5)P$_3$. Experiments were performed as in B and C with relative fluorescence measured at the end of the depolarization step. Error bars represent SEM; the number of independent experiments is noted for each sample.
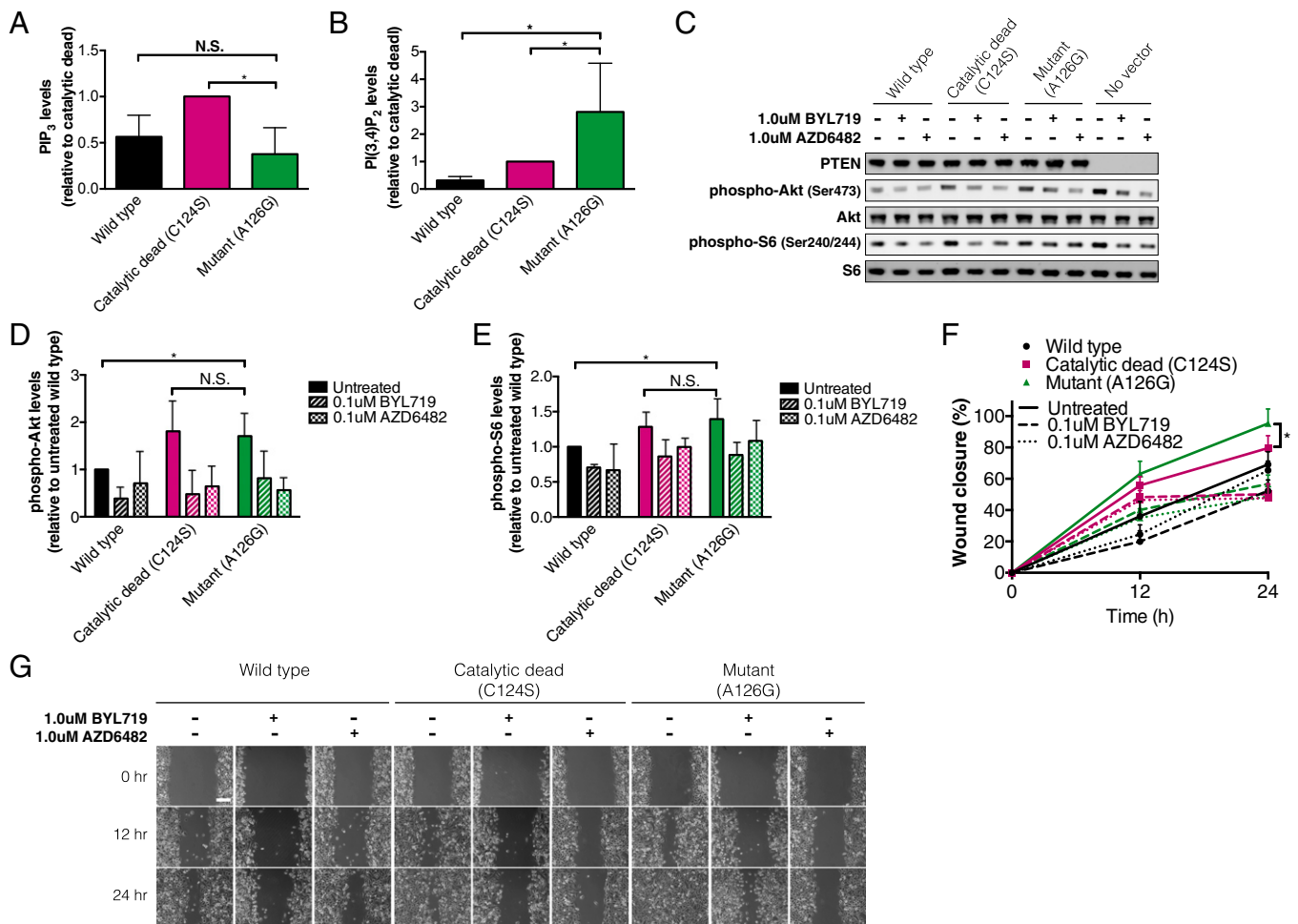
Fig. 3. In vitro characterization of PTEN amino acid 126. (*A* and *B*) Phospholipids were isolated from cell lysates in cells expressing PTEN-WT, PTEN-C124S, or PTEN-A126G. PIP_3 and $PI(3,4)P_2$ levels were quantified by ELISA, and relative abundance was compared with catalytic dead p.C124S expression ($n = 3$). (*A*) There is no statistical significance to the observed difference in PIP_3 between mutant p.A126G and WT alleles (N.S.); however, differences between mutant p.A126G and catalytic dead p.C124S PIP_3 levels are significant (*$P \leq 0.05$). (*B*) Differences in $PI(3,4)P_2$ levels between mutant p.A126G and catalytic dead p.C124S alleles are statistically significant (*$P \leq 0.05$) as are differences between mutant p.A126G and WT alleles (*$P \leq 0.05$). (*C*) Activation of PI3K/Akt pathway in PC-3 cells. Total cell lysates of PC-3 cells transfected with PTEN alleles and drug treated with PI3K-p110α inhibitor (BYL719) or PI3K-p110β inhibitor (AZD6482) were resolved by SDS/PAGE and probed with the indicated antibodies. (*D*) Phospho-Akt levels were normalized over total protein levels and relative abundance was compared with WT expression ($n = 4$). We observed no statistically significant difference between mutant p.A126G and catalytic dead p.C124S mutations (N.S.) but did observe a significant difference between WT and p.A126G protein levels (*$P \leq 0.05$). (*E*) Phospho-S6 levels were normalized over total protein levels, and relative abundance was compared with WT expression ($n = 4$). There is no statistical significance to the difference between mutant p.A126G and catalytic dead p.C124S mutations (N.S.), but the difference between WT and p.A126G protein levels is significant at the *$P \leq 0.05$ level. (*F*) Wound closure was quantified at 0 h, 12 h, and 24 h and normalized relative to 0-h levels using TScratch ($n = 6$). There is a statistical significance between mutant p.A126G and catalytic dead p.C124S at 24 h (*$P \leq 0.05$). (*G*) Assessment of cell migration across PTEN alleles in the presence or absence of the PI3K inhibitor. Representative photographs were taken at 0 h, 12 h, and 24 h postwound. (Scale bar: 200 μm.) Error bars represent SD.

pathway and groupings associated with PI3K/Akt pathway hyperactivation, such as transcriptional and translational activation. Intriguingly, we also found enrichment of processes affiliated with polarized cell migration and projection.

Although PI3K/Akt pathway hyperactivation is also seen in PTEN loss-of-function variants, the up-regulation of $PI(3,4)P_2$ that we observed for PTEN p.A126G (Fig. 2*C* and *SI Appendix*, Fig. *S4D*) is unique to this mutation. Interestingly, increased $PI(3,4)P_2$ levels are thought to promote increased cell migration (22–24). Given these findings and our mass spectrometry data showing enrichment of cell migration processes, we hypothesized that the increased $PI(3,4)P_2$ levels in p.A126G would cause increased cell migration relative to PTEN loss-of-function mutations. To test this hypothesis, we performed scratch wound healing assays on confluent monolayers of cells solely expressing the various PTEN proteins (Fig. 3*G*). We demonstrate that, compared with cells expressing catalytic dead (p.C124S) PTEN, p.A126G PTEN-expressing cells show increased cell migration after 24 h and sensitivity to

intervention with PI3K inhibitors (Fig. 3*F*) ($P \leq 0.05$). To rule out differential cell proliferation rates confounding these results, we performed cell viability, proliferation, and clonogenic cell survival assays across WT, catalytic dead (p.C124S), and mutant (p.A126G) PTEN. We found no statistically significant difference in proliferation between the alleles up to 96 h posttransfection (*SI Appendix*, Figs. S5–S8) although we did note a trend of higher total cell number and colony formation capacity in the mutant (p.A126G) PTEN-expressing cells. These results suggest that p.A126G PTEN expression in cells causes an oncogenic phenotype that sensitizes the cells to PI3K inhibition.

Discussion

Here, we have described an interdisciplinary framework identifying PTEN p.A126G as a top candidate driver mutation and have been able to predict and subsequently demonstrate that the p.A126G mutation produces a novel enzymatic gain-of-function in PTEN from a 3-phosphatase to a 5-phosphatase. Critically, we

GENETICS

find that this changed enzymatic specificity causes an oncogenic increase in $PI(3,4)P_2$ levels at the expense of the $PI(3,4,5)P_3$ concentration. Up-regulation of $PI(3,4)P_2$ is typically associated with increased cell migration (23, 24), and we are able to demonstrate, through global phospho-proteome characterization and in vitro cellular assays, that PTEN p.A126G interferes with cell proliferation pathways and likely even increases the ability of cells to migrate. Contrary to current dogma, these observations suggest that PTEN can also act as an oncogene as well as a tumor suppressor. Lastly, we demonstrate that cells expressing this mutant allele are sensitive to treatment with PI3K inhibitors that are currently undergoing clinical testing (25, 26).

These results add another layer to the findings of PTEN loss-of-function and dominant-negative mutations implicated with tumorigenesis (cf. ref. 13). Taken together, these findings suggest that there is a larger and more complex impact of PTEN mutations on PI3K signaling. Our results highlight the importance of not assuming that all PTEN (or tumor suppressor) mutations produce the same deficient phenotype. It is crucial to look at a patient's mutations on a case-by-case basis to tailor treatment to each individual's variant load and tumor phenotype.

Further studies will be required to better understand whether this gain-of-function is a recurrent mutation and whether PTEN p.A126G mutations can be grouped together therapeutically with other mutations, such as INPP4B loss-of-function mutations (22), that result in increased $PI(3,4)P_2$ levels. These additional studies could potentially provide alternative therapeutic routes for both classes of patients because drugs for one group may not have been considered as viable treatment for the other.

Our unexpected finding suggests that catalytic P-loop mutations in PTEN might have unique effects and that other mutant P-loop residues may display similar gain-of-function properties. Mechanistically, we suggest that increased $PI(3,4)P_2$ levels in the p.A126G PTEN mutant impact cell migration and may modulate tumor migration and metastasis. However, further work is necessary to fully understand the implications of the build up of $PI(3,4)P_2$ and to determine whether other concurrent mutations produce even more pronounced phenotypes.

In summary, by sequencing a single cancer patient and performing a detailed functional characterization of a somatic mutation, we have identified a putatively neomorphic PTEN mutation. Overall, our interdisciplinary approach highlights the complexity of precision cancer medicine in general and provides important insights into novel biology of PI3K/PTEN signaling and PTEN dysfunction.

Methods

Whole-Genome DNA Extraction, Sequencing, and Mapping. We extracted germ-line DNA from saliva and somatic DNA from a fresh frozen prostate tumor biopsy using a Qiagen DNeasy Blood and Tissue DNA Purification kit. Each sample was sequenced on an individual Illumina HiSEq. 2000 lane producing 100-bp paired end reads. We assessed each sequencing run for multiple quality metrics, including number of reads, read quality, and reads mapping to the human genome (*SI Appendix*, Table S1). Sequencing reads were mapped to the human reference genome (hg19) using the BWA mapping algorithm (v 0.6.2) (27). Reads were dynamically trimmed using the "-q" flag to eliminate any nucleotides with Phred quality scores less than 20. Mapped reads were filtered to include only properly paired reads. Tumor and normal mapped pair reads were duplicate-marked via Picard tools (v 1.96) (broadinstitute.github.io/picard/) and underwent joint INDEL realignment and base quality score recalibration using the Genome Analysis Tool Kit (v 2.7–2–g6bda569) (28).

Variant Calling and Annotation. Germ-line SNV and INDEL variant calling was performed using "Unified Genotyper" via the Genome Analysis Tool Kit (v 2.7–2–g6bda569) (28). Somatic SNVs were called using MuTect (v 1.1.4) (29). Somatic INDELs were called using Indelocator (v IndelGenotyper.36.3336), which is within the Genome Analysis Tool Kit (28). Somatic SVs were called using Breakdancer (v 1.2) (30). Somatic CNV calling was done using VarScan (v 2.3.2) (31). All tools were run using the best practices outlined in their respective manuals. Germ-line and somatic variants were annotated for a series of functional predictions, conservation scores, in addition to publically available database annotations using a combination of perl scripts and ANNOVAR (32).

Cells, Drug Compounds, and Plasmids. PC-3 cells were purchased from the American Type Culture Collection and maintained in RPMI 1640 with 10% (vol/vol) FBS, and CHO cells were grown as previously described (17). PI3K-p110α inhibitor BYL719 (Selleckchem) and PI3K-p110β inhibitor AZD6428 (Selleckchem) were dissolved in DMSO. PTEN WT (Addgene plasmid 10750), p.C124S catalytic dead (Addgene plasmid 10744), and p.A126G mutant expression vectors were used for transient transfections into the PC-3 cells. The PTEN p.A126G vector was created by site-directed mutagenesis using the PTEN WT plasmid and the following primers: forward primer, 5′-CTGTAAAGGTG-GAAAGGGACGAACTG-3′; reverse primer, 5′-CCTTTCCACCTTTACAGTGAATTG-CTG-3′. Construction of PTEN$_{CiV}$ chimera (previously named Ci-VSPTEN16) WT was described earlier (19). p.C124S catalytic dead, p.A126G, p.A126P, p.A126V, and p.A126S mutant plasmids were created by site-directed mutagenesis using the QuikChange II XL Site-Directed Mutagenesis Kit (Agilent Technologies). All sequences were verified before use (Seqlab Sequence Laboratories).

Expression vectors used for transfection of CHO cells were as follows: PLCδ$_1$-PH (UniProt accession number P51178) or Btk-PH (Q06187) in pEGFP-N1 vector; TAPP1 (Q9HB21) in FUGW vector (contains eGFP); bovine phosphatidylinositol 3-kinase p110α (constitutively active mutant K227E; P32871) (33) in pcDNA3; and PTEN$_{CiV}$ chimera and mutants in mRFP-C vector.

Transfections. Twenty-four hours before transfection, PC-3 cells were plated at a density of 1.5×10^5 cells per well in six-well plates. The PC-3 cells were then transfected with 1.5 μg of vector DNA complexed with 5 μL of Lipofectamine 3000 (Life Technologies) in accordance with the manufacturer's Lipofectamine 3000 protocol. CHO cells were plated onto glass bottom dishes (WillCo Wells B. V.) or coverslips 24–48 h before transfection, which was performed using jetPEI (Polyplus Transfection) in accordance with the manufacturer's instructions. All experiments on CHO cells were performed 24–48 h after transfection.

Whole-Cell Patch Clamp and Fluorescence Microscopy. For total internal reflection fluorescence (TIRF) experiments, the whole cell configuration of the patch clamp technique was used using an EPC-10 amplifier controlled by PatchMaster software (HEKA Elektronik). CHO cells were clamped to –60 mV, and chimeras were activated by depolarizing the cell to 80 mV for 30 s. In these experiments, series resistance (R_s) typically was below 5 MΩ, and no R_s compensation was applied. Patch pipettes were pulled from borosilicate glass using a P2000 puller (Sutter Instrument Company), and they had an open pipette resistance between 2 and 4 MΩ after back-filling with intracellular solution containing 135 mM KCl, 2.41 mM CaCl$_2$, 3.5 mM MgCl$_2$, 5 mM EGTA, 5 mM Hepes, and 2.5 mM Na$_2$-ATP, pH 7.3 (with KOH), 290–295 mosm/kg. Throughout the recordings, cells were kept in extracellular solution containing 144 mM NaCl, 5.8 mM KCl, 0.9 mM MgCl$_2$, 1.3 mM CaCl$_2$, 0.7 mM NaH$_2$PO$_4$, 5.6 mM D-glucose, 10 mM Hepes, pH 7.4 (with NaOH), 305–310 mosm/kg. All experiments were performed at room temperature (22–25 °C).

TIRF imaging was done as described before (17). Briefly, a BX51WI upright microscope (Olympus) equipped with a TIRF-condenser (N.A. 1.45; Olympus) and a 488-nm laser (20 mW; Picarro) was used. Fluorescence was imaged through a LUMPlanFI/IR 40×/0.8 N.A. water-immersion objective. Images were acquired with a TILL-Imago QE cooled CCD camera (TILL Photonics) in combination with a Polychrome IV light source (TILL Photonics) controlled by TILLvision software (TILL Photonics). The frame interval was 3 s, and the laser shutter was controlled by the Polychrome IV. The electrophysiology setup was synchronized to the imaging setup. Cells were cotransfected with plasmids coding for an mRFP-tagged phosphatase, a PI sensor domain, and, for experiments involving sensors for $PI(3,4)P_2$ or $PI(3,4,5)P_3$, additionally p110α(K227E). Experiments were done 24–48 h posttransfection on cells selected for expression of the mRFP tag. Cells under investigation were whole cell patch clamped as described above. Experiments were carried out at room temperature (22–25 °C). Imaging data were analyzed using TILLvision (Till Photonics) and IgorPro (Wavemetrics). Regions of interest (ROIs) encompassed the footprint of a single cell, excluding cell margins to avoid movement artifacts. F/F_0 traces were calculated from the background-corrected TIRF signal intensity F, normalized pixelwise to the initial intensity F_0, which was calculated as the average over the baseline interval, by averaging over the ROI. F/F_0 traces were corrected for bleaching according to mono-exponential fits to the baseline interval as described previously (19).

$PI(3,4,5)P_3$ and $PI(3,4)P_2$ Quantification. Transfected PC-3 cells were seeded at a density of 2×10^6 cells per 15-cm dish for $PI(3,4,5)P_3$ and $PI(3,4)P_2$ extractions, respectively. At 80% confluence, the media was aspirated, and 10 mL of ice cold 0.5 M TCA was immediately added. After a 5-min incubation on ice, cells were scraped, transferred to a 15-mL centrifuge tube, and spun at $300 \times g$ for 5 min. The pellet was resuspended in 3 mL of 5% trichloroacetic acid/1 mM EDTA and centrifuged at $300 \times g$ for 5 min, and the supernatant was discarded. Neutral lipids were extracted by adding 3 mL of methanol:chloroform (2:1), vortexing

three times over 10 min at room temperature, centrifuging at $300 \times g$ for 5 min, and discarding the supernatant. Acidic lipids were extracted by adding 2.25 mL of methanol:chloroform:12M hydrochloric acid (80:40:1) to the pellet, resuspending, vortexing four times over 15 min at room temperature, centrifuging at $300 \times g$ for 5 min, and transferring the supernatant to a new 15-mL centrifuge tube. Then 0.75 mL of methanol and 1.35 mL of 0.1 M hydrochloric acid were added to the supernatant, vortexed, centrifuged at $300 \times g$ for 5 min to separate organic and aqueous phases. The organic (lower) phase was collected into a new vial and dried in a vacuum dryer for 1 h. Samples were suspended in 65 mL of PBS-Tween+3% Protein Stabilizer (provided by the Echelon kit), vortexed, and spun down before adding to the ELISA. PI(3,4,5)P$_3$ and PI(3,4)P$_2$ phospholipid quantification was performed according to the manufacturer's instructions respective to each kit (K-2500s and K-3800; Echelon Biosciences).

Immunoblotting. Whole cell protein lysates were extracted from PC-3 cells 24 h after transfection. Six micrograms of whole cell lysates were loaded into polyacrylamide gels and subjected to SDS/PAGE electrophoresis. Nitrocellulose membranes were incubated with anti-PTEN, anti-S6, anti-Phospho-S6, anti-Akt, or anti-Phospho-Akt (nos. 9559, 2217, 2215, 4691, and 4060, respectively; Cell Signaling Technology). All antibodies were diluted 1:1,200 in Tris-buffered saline and Tween 20 with 5% BSA. Goat anti-rabbit IgG (H+L) labeled with IRDye 680RD conjugate (Licor) was used as a secondary antibody. Bands were detected using a Licor ODYSSEY fluorescent imaging system.

Wound-Healing Assays. Before seeding with cells, auxiliary lines used as reference points for imaging the wound were drawn on the underside of each well of a six-well plate. Plates were seeded at a density of 1.5×10^5 cells per well and allowed to grow for 48 h. Cells were transfected, and a linear wound was applied to the monolayer using a 200-μL pipette tip 24 h later. Loose cells were removed with three washes of PBS. Drugs, if any, were added to the cells, and images were captured immediately after wounding (T$_0$) and subsequently in 12-h intervals (T$_{12}$, and T$_{24}$). TScratch was used to calculate percentage of wound closure (34).

Cell Proliferation Assays. Cells were transfected with PTEN WT, catalytic dead (p.C124S), or mutant (p.A126G) plasmids. Six-well plates were seeded with PC-3 cells at a density of 5×10^4 cells per well and allowed to grow for 96 h. Presto blue (Life Technologies) was added to each well after the 96-h posttransfection

incubation. After a 2-h incubation with presto blue, dye absorbance was measured on a Tecan Infinite 200 PRO plate reader at 570 nm and a reference wavelength of 600 nm. Measured absorbance values were normalized by absorbance at the reference wavelength.

Total Cell Number Assays. Cells were transfected with PTEN WT, catalytic dead (p.C124S), or mutant (p.A126G) plasmids. Six-well plates were seeded with PC-3 cells at a density of 5×10^4 cells per well and allowed to grow for 96 h. Then 1 mL of 0.05% Trypsin-EDTA was added for 5 min to detach cells, followed by the addition of 3 mL of media to resuspend the detached cells. Total cell number was measured using a Scepter 2.0 Handheld Automated Cell Counter (EMD Millipore).

Clonogenic Cell Survival Assays. Cells were transfected with PTEN WT, catalytic dead (p.C124S), or mutant (p.A126G) plasmids. After a 96-h posttransfection incubation period, six-well plates were seeded with PC-3 cells at a density of 200 cells per well and allowed to grow for 21 d. Media was then gently aspirated, 3 mL of methylene blue was added for 30 min, the methylene blue was then gently aspirated, and the six-well plates were allowed to dry at room temperature for 30 min. Individual colonies were then counted using a Fischerbrand Counter Pen (Fischer Scientific).

Statistical Analysis. All statistical analyses were performed in the R programming language. Statistical significance was determined by the Student's t test for comparisons between groups and one-way ANOVA followed by a post hoc Tukey's honest significant difference test for pairwise comparisons across all groups.

1. Forbes SA, et al. (2011) COSMIC: Mining complete cancer genomes in the Catalogue of Somatic Mutations in Cancer. *Nucleic Acids Res* 39(Database issue):D945–D950.
2. Weinstein JN, et al.; Cancer Genome Atlas Research Network (2013) The Cancer Genome Atlas Pan-Cancer analysis project. *Nat Genet* 45(10):1113–1120.
3. Alexandrov LB, et al.; Australian Pancreatic Cancer Genome Initiative; ICGC Breast Cancer Consortium; ICGC MMML-Seq Consortium; ICGC PedBrain (2013) Signatures of mutational processes in human cancer. *Nature* 500(7463):415–421.
4. Nik-Zainal S, et al.; Breast Cancer Working Group of the International Cancer Genome Consortium (2012) Mutational processes molding the genomes of 21 breast cancers. *Cell* 149(5):979–993.
5. Peifer M, et al. (2012) Integrative genome analyses identify key somatic driver mutations of small-cell lung cancer. *Nat Genet* 44(10):1104–1110.
6. Ellis MJ, et al. (2012) Whole-genome analysis informs breast cancer response to aromatase inhibition. *Nature* 486(7403):353–360.
7. Craig DW, et al. (2013) Genome and transcriptome sequencing in prospective metastatic triple-negative breast cancer uncovers therapeutic vulnerabilities. *Mol Cancer Ther* 12(1):104–116.
8. Demeure MJ, et al. (2014) Whole-genome sequencing of an aggressive BRAF wild-type papillary thyroid cancer identified EML4-ALK translocation as a therapeutic target. *World J Surg* 38(6):1296–1305.
9. Chen Z, et al. (2005) Crucial role of p53-dependent cellular senescence in suppression of Pten-deficient tumorigenesis. *Nature* 436(7051):725–730.
10. Maehama T, Dixon JE (1998) The tumor suppressor, PTEN/MMAC1, dephosphorylates the lipid second messenger, phosphatidylinositol 3,4,5-trisphosphate. *J Biol Chem* 273(22):13375–13378.
11. Maehama T, Taylor GS, Dixon JE (2001) PTEN and myotubularin: Novel phosphoinositide phosphatases. *Annu Rev Biochem* 70:247–279.
12. Alimonti A, et al. (2010) Subtle variations in Pten dose determine cancer susceptibility. *Nat Genet* 42(5):454–458.
13. Papa A, et al. (2014) Cancer-associated PTEN mutants act in a dominant-negative manner to suppress PTEN protein function. *Cell* 157(3):595–610.
14. Murata Y, Iwasaki H, Sasaki M, Inaba K, Okamura Y (2005) Phosphoinositide phosphatase activity coupled to an intrinsic voltage sensor. *Nature* 435(7046):1239–1243.
15. Hossain MI, et al. (2008) Enzyme domain affects the movement of the voltage sensor in ascidian and zebrafish voltage-sensing phosphatases. *J Biol Chem* 283(26):18248–18259.
16. Ratzan WJ, Evsikov AV, Okamura Y, Jaffe LA (2011) Voltage sensitive phosphoinositide phosphatases of Xenopus: Their tissue distribution and voltage dependence. *J Cell Physiol* 226(11):2740–2746.
17. Halaszovich CR, Schreiber DN, Oliver D (2009) Ci-VSP is a depolarization-activated phosphatidylinositol-4,5-bisphosphate and phosphatidylinositol-3,4,5-trisphosphate 5′-phosphatase. *J Biol Chem* 284(4):2106–2113.
18. Lee JO, et al. (1999) Crystal structure of the PTEN tumor suppressor: Implications for its phosphoinositide phosphatase activity and membrane association. *Cell* 99(3):323–334.
19. Lacroix J, et al. (2011) Controlling the activity of a phosphatase and tensin homolog (PTEN) by membrane potential. *J Biol Chem* 286(20):17945–17953.
20. Halaszovich CR, et al. (2012) A human phospholipid phosphatase activated by a transmembrane control module. *J Lipid Res* 53(11):2266–2274.
21. Knight ZA, et al. (2006) A pharmacological map of the PI3-K family defines a role for p110α in insulin signaling. *Cell* 125(4):733–747.
22. Gewinner C, et al. (2009) Evidence that inositol polyphosphate 4-phosphatase type II is a tumor suppressor that inhibits PI3K signaling. *Cancer Cell* 16(2):115–125.
23. Yamaguchi H, Oikawa T (2010) Membrane lipids in invadopodia and podosomes: Key structures for cancer invasion and metastasis. *Oncotarget* 1(5):320–328.
24. Yamaguchi H, et al. (2011) Phosphoinositide 3-kinase signaling pathway mediated by p110α regulates invadopodia formation. *J Cell Biol* 193(7):1275–1288.
25. Furet P, et al. (2013) Discovery of NVP-BYL719 a potent and selective phosphatidylinositol-3 kinase alpha inhibitor selected for clinical evaluation. *Bioorg Med Chem Lett* 23(13):3741–3748.
26. Nylander S, et al. (2012) Human target validation of phosphoinositide 3-kinase (PI3K)β: Effects on platelets and insulin sensitivity, using AZD6482 a novel PI3Kβ inhibitor. *J Thromb Haemost* 10(10):2127–2136.
27. Li H, Durbin R (2009) Fast and accurate short read alignment with Burrows-Wheeler transform. *Bioinformatics* 25(14):1754–1760.
28. DePristo MA, et al. (2011) A framework for variation discovery and genotyping using next-generation DNA sequencing data. *Nat Genet* 43(5):491–498.
29. Cibulskis K, et al. (2013) Sensitive detection of somatic point mutations in impure and heterogeneous cancer samples. *Nat Biotechnol* 31(3):213–219.
30. Chen K, et al. (2009) BreakDancer: An algorithm for high-resolution mapping of genomic structural variation. *Nat Methods* 6(9):677–681.
31. Koboldt DC, et al. (2012) VarScan 2: Somatic mutation and copy number alteration discovery in cancer by exome sequencing. *Genome Res* 22(3):568–576.
32. Wang K, Li M, Hakonarson H (2010) ANNOVAR: Functional annotation of genetic variants from high-throughput sequencing data. *Nucleic Acids Res* 38(16):e164.
33. Rodriguez-Viciana P, Warne PH, Vanhaesebroeck B, Waterfield MD, Downward J (1996) Activation of phosphoinositide 3-kinase by interaction with Ras and by point mutation. *EMBO J* 15(10):2442–2451.
34. Gebäck T, Schulz MMP, Koumoutsakos P, Detmar M (2009) TScratch: A novel and simple software tool for automated analysis of monolayer wound healing assays. *Biotechniques* 46(4):265–274.

GENETICS